nature communications

Article

https://doi.org/10.1038/s41467-025-59980-z

Cation-self-shielding strategy promises high-voltage all-Prussian-blue-based aqueous K-ion batteries

Received: 4 January 2024

Accepted: 9 May 2025

Published online: 21 May 2025

Check for updates

Qiubo Guo[1,2,3,7], Shuai Han[1,2,7], Yaxiang Lu[1,4,5] ✉, Ruijuan Xiao[1,5] ✉, Jin Li[6], Qingli Hao[3], Xiaohui Rong[1,5], Suting Weng[1,2], Yaoshen Niu[1], Feixiang Ding[1,4], Yang Yang[1,2], Hui Xia[6], Xuefeng Wang[1], Fei Xie[1], Lin Zhou[1], Xueyan Hou[1], Hong Li[1,2,4,5], Xuejie Huang[1], Liquan Chen[1] & Yong-Sheng Hu[1,2,4,5] ✉

Prussian blue analogues (PBAs) are promising electrode candidates for aqueous batteries because the inevitable interstitial water is generally thought to have little impact on battery performance. Currently, mounting researches have focused on optimizing PBA properties by varying transition metal composition, but less attention has been paid to interstitial water, especially in alkali metal-ion deficient PBAs with large cavities. Here, we employ the water-rich $K_{0.01}Mn[Cr(CN)_6]_{0.74}\cdot 4.75H_2O$ as the negative electrode to study the effect of interstitial water. It is found that during de-potassiation, the electrode undergoes dehydration, which negatively impacts kinetics, distorts structure, and raises charging potential. A cation-self-shielding strategy involving Dihydroxyacetone (DHA) in the electrolyte to secure the water-rich state is then proposed. The built 1.82 V all-Prussian blue aqueous K-ion battery delivers a high practical specific energy of ~76 Wh kg^{-1} over 1.5 V (based on the total mass of active materials in both electrodes). This study reveals the significance of interstitial water on the kinetics of PBA negative electrodes and promotes the exploration of water-containing electrodes to develop high-voltage aqueous rechargeable batteries for energy storage applications.

Prussian blue analogs (PBAs), possessing the advantages of robust structure, diverse physiochemical properties, sustainable synthesis process, and good compatibility with aqueous electrolytes, are regarded as appealing electrode candidates for aqueous batteries[1–4]. However, traditional efforts to optimize PBA electrodes mainly focus on modifying the crystal structure and transition metals, while ignoring the effects of the inherent crystal water on electrochemical behaviors[5,6]. Notably, PBAs can have abundant crystal water occupying the large cavities, which may affect the kinetics and thermodynamics of the electrodes and complicate their compatibility with aqueous batteries[7,8]. Therefore, it is significant to explore the effects of interstitial water on the

[1]Key Laboratory for Renewable Energy, Beijing Key Laboratory for New Energy Materials and Devices, Beijing National Laboratory for Condensed Matter Physics, Institute of Physics, Chinese Academy of Sciences, Beijing, China. [2]College of Materials Science and Optoelectronic Technology, University of Chinese Academy of Sciences, Beijing, China. [3]Key Laboratory for Soft Chemistry and Functional Materials, Ministry of Education, School of Chemical Engineering, Nanjing University of Science and Technology, Nanjing, P. R. China. [4]Huairou Division, Institute of Physics, Chinese Academy of Sciences, Beijing, China. [5]Yangtze River Delta Physics Research Center Co. Ltd, Liyang, China. [6]Herbert Gleiter Institute of Nanoscience, School of Materials Science and Engineering, Nanjing University of Science and Technology, Nanjing, China. [7]These authors contributed equally: Qiubo Guo, Shuai Han.
✉e-mail: yxlu@iphy.ac.cn; rjxiao@iphy.ac.cn; yshu@iphy.ac.cn

electrochemical behavior of PBAs in order to fully realize their potential in aqueous batteries[9,10].

It has already been found that the crystal water in the electrode framework structure plays a favorable role in aqueous batteries. For example, the crystal water can stabilize the structure of A-birnessite ($A_xMnO_2{\cdot}yH_2O$, where A represents Na^+, Mg^{2+}, etc.) materials and the hydrated PBAs can facilitate Grotthuss proton conduction during redox reactions[11–13]. Additionally, exploring the relationship between crystal water and electrode behavior can help to improve and enhance deficient electrode systems in aqueous batteries that are facing a lack of usable electrodes. Some studies have demonstrated that the crystal water within the interlayer of disordered $K_{0.22}V_{1.74}O_{4.37}$ and P3-$K_{0.4}Fe_{0.1}Mn_{0.8}Ti_{0.1}O_2$ can improve the stability and rate performance of these electrodes to make them compatible with aqueous electrolytes[14,15]. However, the effects of crystal water in PBAs with varying amounts of interstitial water, which are the most promising electrode candidates for aqueous alkali metal-ion batteries, are not yet fully understood.

Among various PBA materials[16–21], PBA negative electrodes with alkali metal-ion deficiency and large cavities provide more opportunities for the invasion of interstitial water, which will severely affect the electrochemical properties. Meanwhile, the structural merits and low-potential superiority of PBA negative electrodes offer an opportunity for achieving high-voltage aqueous batteries with high specific energy[20,21], particularly for aqueous K-ion batteries (AKIBs), which are commonly using traditional organic[5,17,19] and $KTi_2(PO_4)_3$[18] with high charging potential, low capacity, or extremely low initial Coulombic efficiency as negative electrode materials. However, to our knowledge, there has been no study on PBA negative electrodes in AKIBs and the effect of their interstitial water, let alone the impact of the de-solvation process that may arise from the small Stokes radius of solvated K^+ ions[22,23], which is worth exploring in this field.

Herein, manganese hexacyanochromate $Mn[Cr(CN)_6]_{1-z}\square_z{\cdot}mH_2O$ PBA negative electrodes with large cavities were selected and purposely synthesized with different interstitial water contents to study effects of interstitial water, namely the water-rich $K_{0.01}Mn[Cr(CN)_6]_{0.74}{\cdot}4.75H_2O$ (MnHCC) and water-poor $K_{0.01}Mn[Cr(CN)_6]_{0.74}{\cdot}1.89H_2O$ (MnHCC-D). It is found for MnHCC negative electrodes that the capacity fading occurs with the cycling process, and the initial single charging plateau splits into two to keep raising the average charging potential, similar to the initial performance of MnHCC-D, indicating the dehydration of interstitial water in the structure and the deteriorated kinetics during the de-potassiation process. To address this problem, a small molecule of dihydroxyacetone (DHA) was deliberately added into the 21 m KCF_3SO_3 (21KOTF) electrolyte to impede the dehydration process. Due to the stronger chemical coordination of K^+ with DHA than with H_2O, the newly formed self-shielding K^+-DHA ions can alleviate the invasion of the interstitial water into the solvation shell of K^+ ions, reserving the interstitial water in the structure to sustain the kinetics and structural stability of the negative electrode. The MnHCC negative electrode in the modified electrolyte demonstrates almost theoretical capacity with a maintained average charging potential at around −1.0 V. The built all-PBA-based AKIBs realizes a high voltage of 1.82 V and delivers a high specific energy of 82 Wh kg^{-1}. This study reveals the significance of interstitial water in sustaining the structural framework and facilitating charge transportation, and successfully maintains them via the proposed cation-self-shielding strategy, redefining the electrochemical behavior of the water-rich PBA negative electrodes and offering a direction for the practical application of high-voltage AKIBs.

Results

Electrochemical performance and proposed storage mechanism

The MnHCC sample was synthesized by the simple co-precipitation method and then dried in air at room temperature. For comparison, samples purposely dried at 100 °C are denoted as MnHCC-D. The X-ray diffraction (XRD) patterns of MnHCC and MnHCC-D demonstrate the same cubic phase (space group: Fm-3m) but different crystallinities, which is further confirmed by the refined result for MnHCC (Supplementary Figs. 1 and 2 and Supplementary Table 1). According to images of the scanning electron microscopy (SEM, Supplementary Fig. 3), the surface of MnHCC is smoother than that of MnHCC-D. The thermal gravimetric (TG), derivative thermal gravimetric (DTG), and inductively coupled plasma atomic emission spectrometry (ICP-AES) analyses are used to confirm the stoichiometric compositions of MnHCC and MnHCC-D, which are verified as $K_{0.01}Mn[Cr(CN)_6]_{0.74}{\cdot}4.75H_2O$ and $K_{0.01}Mn[Cr(CN)_6]_{0.74}{\cdot}1.89H_2O$, notably, the MnHCC sample is indeed rich in interstitial water (Supplementary Fig. 4, Supplementary Tables 2 and 3, and related discussions).

The electrochemical properties were evaluated using three-electrode cells with Ag/AgCl as the reference electrode. Galvanostatic charge–discharge (GCD) curves of MnHCC are recorded in the 21KOTF electrolyte at a current rate of 300 mA g^{-1} (Fig. 1a). An average reversible capacity of 67.4 mAh g^{-1} with symmetric charging–discharging plateaus at the potential of -1.0 V is observed, which is higher than that of 44 mAh g^{-1} for the MnHCC-D electrode. However, along with cycling, a new charging plateau appears at a higher potential of −0.8 V, and the capacity ratio of the higher plateau to the lower plateau keeps rising in the following cycles. The low current rate (150 mA g^{-1}) even accelerates the appearance of the higher charging plateau in the first cycle (Supplementary Fig. 5). This phenomenon also occurs in the 21 m KFSI and 1 m KOTF (1KOTF) electrolytes (Supplementary Figs. 6–8 and related discussion), suggesting it is independent of the K-based salt and concentration in the electrolytes.

The appeared high charging plateau definitely decreases the average discharging voltage and specific energy of full cells but we are reluctant to relate it to the phase transition since no symmetric plateaus are shown in the discharging processes[24–26]. The ex situ XRD results of the cycled MnHCC/-D electrodes can further support the conception (Supplementary Fig. 9 and related discussion). Coincidently, we found the GCD curve of MnHCC after cycling is similar to that of the MnHCC-D, where the charging plateau climbs to a higher potential and the cycled MnHCC/-D electrodes demonstrate the same cubic phase (Supplementary Fig. 10). Based on these results, we propose a hypothesis that the gradually increased high-potential plateau relates to the gradual loss of interstitial water in the negative electrode skeleton, where the intercalated K^+ ions will coordinate to the interstitial water molecules and carry them out during the de-potassiation process. Regarding the charging process, the early dehydration process enhances the ion-diffusion barrier of the subsequent de-potassiation process to push the latter half of the charging plateau to a higher potential[27]. However, after the fully charged process, the remaining interstitial water molecules in MnHCC return to uniform distribution under diffusion, and the discharging process maintains the single plateau with less potential hysteresis than the charging process, thus resulting in asymmetric GCD curves. Kinetic analysis results by galvanostatic intermittent titration technique (GITT) further demonstrate the serious potential hysteresis and the slow kinetics of MnHCC during the charging process (Supplementary Fig. 11 and related discussion).

To impede the dehydration process, an armor of K^+ needs to be constructed to prevent the invasion of interstitial water and maintain the water-rich environment of the MnHCC framework. Since the solvation of K^+ in aqueous solution mainly arises from its interaction with the oxygen in H_2O, we intended to introduce an additive into the 21KOTF electrolyte, which contains oxygen functional groups[28], and can preferentially occupy the solvation shell of K^+ to co-intercalate into the MnHCC electrode. The stronger chemical coordination of K^+ with the additive than with H_2O helps repel the interstitial water during the de-intercalation process. Given the above considerations, several small molecules such as EG[29], glycerol[30], acetone[31], glucose[32],

https://doi.org/10.1038/s41467-025-59980-z

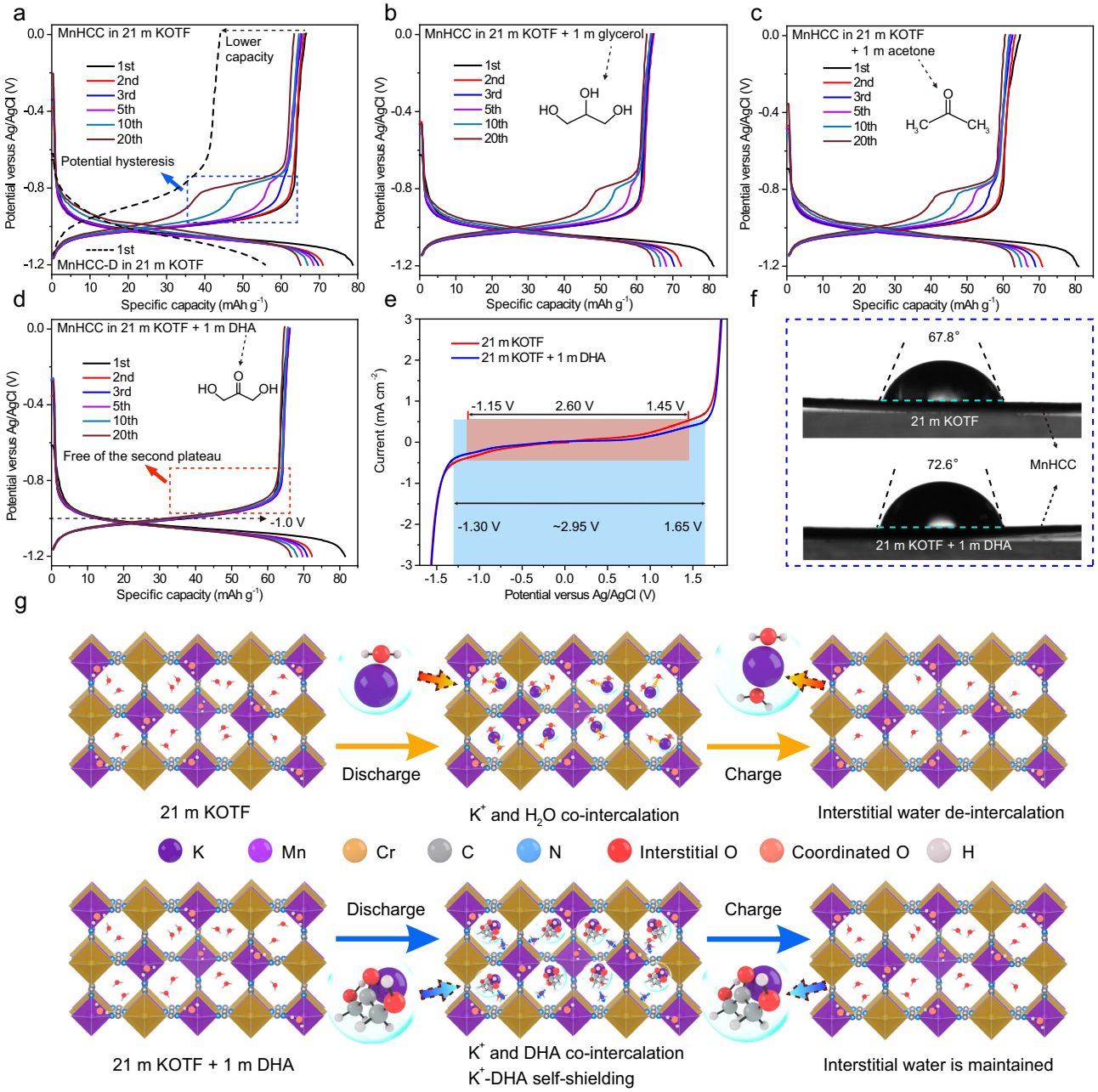

Fig. 1 | Electrochemical performance and schematic illustration. GCD curves of the MnHCC and MnHCC-D electrodes in the 21KOTF electrolytes at 300 mA g^{-1} (**a**). GCD curves of the MnHCC electrodes in the 21KOTF + 1 m glycerol (**b**), 21KOTF + 1 m acetone (**c**), and 21KOTF + 1 m DHA (21KOTF-1DHA) (**d**) electrolytes at 300 mA g^{-1}. The electrochemical properties were evaluated using three-electrode cells at 27 °C, where activated carbon (AC) and Ag/AgCl served as the counter and reference electrodes, respectively. The mass loading of the working electrodes is around 30 mg cm^{-2} and the potential is not iR-corrected. **e** Linear sweep voltammetry (LSV) curves are recorded on titanium mesh at 10 mV s^{-1} in the 21KOTF and 21KOTF-1DHA electrolytes with different shadowed areas representing different potential ranges. **f** The contact angles of the 21KOTF and 21KOTF-1DHA electrolytes. **g** Schematic illustration of the discharging-charging processes of the MnHCC electrodes in the 21KOTF and 21KOTF-1DHA electrolytes.

and DHA, which contain carbonyl, more hydroxyl or both of them, were added to the electrolyte to occupy the solvation shell of K^+ and tested GCD curves (Fig. 1b–d and Supplementary Fig. 12). Only glucose and DHA, which contain both hydroxyl and carbonyl groups, could significantly inhibit the appearance of the high-potential plateau. Considering the higher weight of glucose than DHA, we finally chose 21KOTF + 1 m DHA (21KOTF-1DHA) as the optimal electrolyte (Supplementary Figs. 13 and 14 and related discussion), and the GITT profiles of the electrode demonstrate negligible potential hysteresis during the charging–discharging processes (Supplementary Fig. 15).

To investigate the different electrochemical properties of the 21KOTF and 21KOTF-1DHA electrolytes, we measured the voltage windows (Fig. 1e). The introduction of the DHA widened the voltage window of the 21KOTF electrolyte, significantly, which is favorable to the low operation potential of the MnHCC electrode. The formation of the solid electrolyte interphase (SEI) arising from the decomposition of the OTF^- anions on the negative electrode side could further alleviate the potential hydrogen evolution reactions (HER). Meanwhile, the increased contact angle of the 21KOTF-1DHA electrolyte could suppress the dissolution of MnHCC to some extent with improved electrochemical stability (Fig. 1f).

https://doi.org/10.1038/s41467-025-59980-z

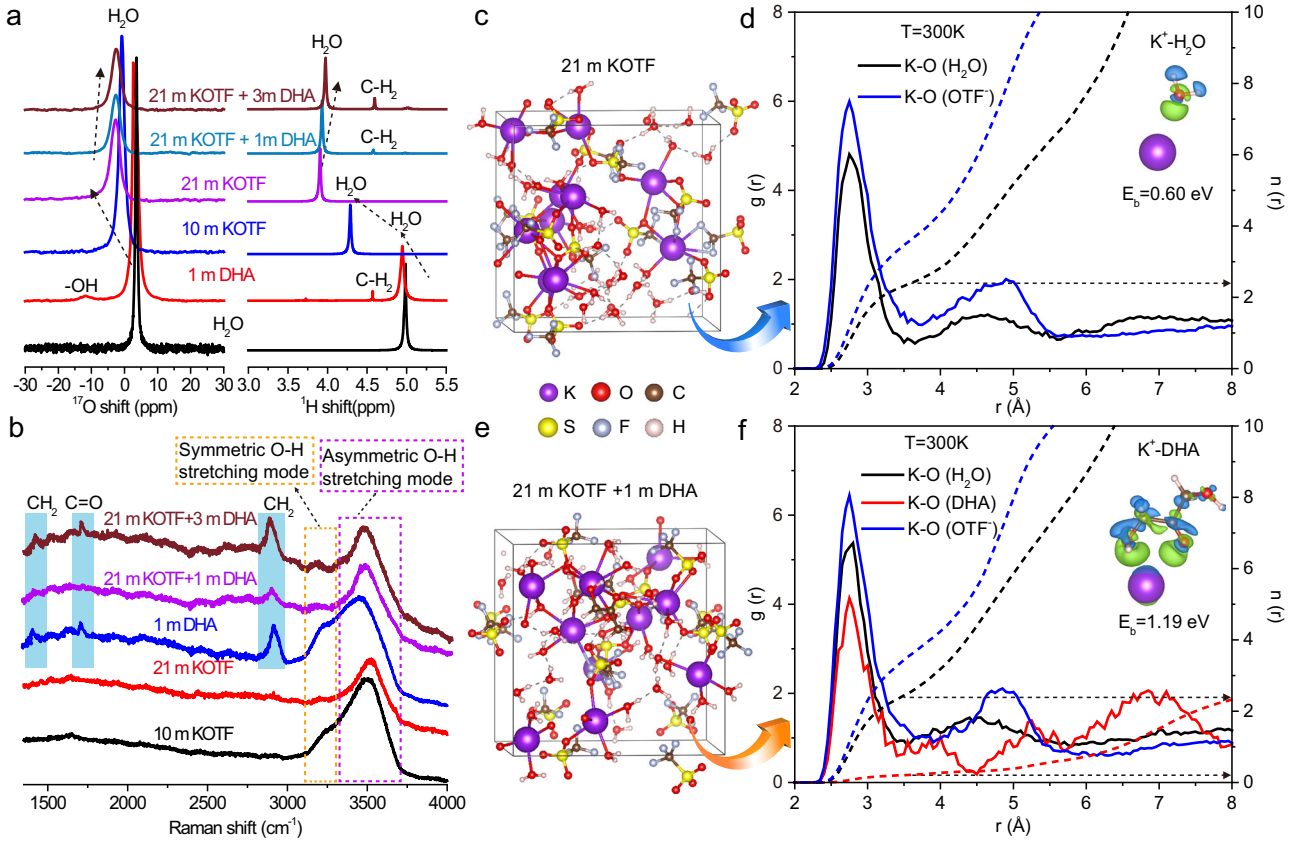

Fig. 2 | Characterizations and AIMD simulations of different electrolyte solutions. a ^{17}O and ^{1}H NMR spectra of H_2O in different aqueous solutions. **b** Raman spectra for different aqueous solutions with shadowed areas representing different peaks. 3D snapshots of the 21KOTF (**c**) and 21KOTF-1DHA (**e**) electrolytes from AIMD simulations. The RDFs and coordination numbers of K with O-atom from H_2O, OTF^-, or DHA in the 21KOTF (**d**) and 21KOTF-1DHA (**f**) electrolytes from AIMD simulations (300 K); the insets in (**d**, **f**) are the binding energies (E_b) of K^+-H_2O and K^+-DHA, respectively. Similar AIMD simulation results were also obtained at 500 K (Supplementary Fig. 25).

We further measured cyclic voltammetry (CV) and in situ galvanostatic electrochemical impedance spectra (GEIS) with distribution of relaxation time (DRT) analysis of the MnHCC electrodes in the 21KOTF and 21KOTF-1DHA electrolytes (Supplementary Figs. 16–18 and related discussions), which are corresponding to the above GCD curves and GITT conclusions. Besides, the optimal 21KOTF-1DHA electrolyte also endows an improved cycling performance (Supplementary Fig. 19), which may arise from the maintained water-rich environment and robust structure of the MnHCC.

Figure 1g schematically illustrates the assumed charging–disc harging processes of the MnHCC electrodes in two electrolytes. In the 21KOTF electrolyte, the main cation species are K^+-xH_2O ions. During the potassiation process, after partial de-solvation, K^+-$(x\text{-}y)H_2O$ ions intercalate into the electrode and couple with the interstitial water molecules. Then the newly formed K^+-$(x\text{-}y+z)H_2O$ ions de-intercalate from the electrode structure during the de-potassiation process. The decreased interstitial water could weaken the kinetics of the electrode and exacerbate the cubic-structure distortion during the following cycles. By contrast, in the 21KOTF-1DHA electrolyte, K^+ ions have stronger chemical coordination with DHA molecules than with H_2O and the formed self-shielding K^+-DHA species could co-intercalate into the electrode. The DHA molecule may not only act as the armor of the K^+ ion to prevent the invasion of the interstitial water into the solvation shell but also sustain the electrode structure. Then the K^+-DHA species de-intercalate from the electrode during the charging process with interstitial water remaining in the electrode structure. Therefore, the 21KOTF-1DHA electrolyte could improve the electrochemical stability of the MnHCC electrode significantly. In addition, we synthesized the cubic zinc hexacyanochromate (ZnHCC) sample (Supplementary Fig. 20 and Supplementary Table 4), and GCD curves of the ZnHCC electrodes in the 21KOTF and 21KOTF-1DHA electrolytes further verify the dehydration problem and cation-self-shielding strategy (Supplementary Fig. 21 and related discussion). The strategy also works in diluted electrolyte (Supplementary Figs. 22 and 23 and related discussion). To verify the hypothetical mechanism, we will figure out three questions in the following parts: (1) configurations of the primary cation species in the two electrolytes and the function of the DHA additive; (2) the interaction between the intercalated cations and the interstitial water; (3) the structural changes of the electrode during the de-/potassiation processes.

Configurations and performance of the electrolytes

To figure out the configuration of the primary cation species in the electrolytes and the function of DHA additive, nuclear magnetic resonance (NMR) spectroscopy was carried out to investigate the structural environments of the ion species in different solutions, and the results are shown in Fig. 2a and Supplementary Fig. 24. The ^{17}O signals of H_2O in 1 m DHA, 10 m, and 21 m KOTF solutions demonstrate the lowered chemical shift from 2.64 ppm to −0.76, and −2.65 ppm, respectively, which can be attributed to the decrease of free water. Along with the increase in DHA concentration, the ^{17}O signal shifts up to −2.54 and −2.43 ppm. Similarly, the ^{1}H peaks of H_2O in 1 m DHA, 10 m, and 21 m KOTF solutions shift from 4.95 ppm to 4.29, and 3.90 ppm, then move to 3.93 and 3.98 ppm in 21KOTF + 1 and 3 m DHA solutions, respectively. These results suggest that the introduction of DHA can weaken the solvation interaction between K^+ and H_2O[28,33].

Besides, the ^{17}O signal of -OH from 1 m DHA disappears in 21KOTF + 1 and 3 m DHA solutions, indicating the interaction between DHA and K^+, which supports the existence of the K^+-DHA species probably exist in the 21KOTF-1DHA electrolyte.

To further understand the function of DHA in the 21KOTF-1DHA electrolyte, Raman spectroscopy was conducted to analyze the different solutions (Fig. 2b). Compared to the 10 and 21 m KOTF, the peak of C = O (1737 cm^{-1}) appears in the 1 m DHA solution[34], but it disappears in the 21KOTF-1DHA solution, which suggests the interaction between C = O and K^+. Moreover, 1 m DHA and 10 m KOTF show two broad peaks at around 3209 and 3507 cm^{-1}, which can be ascribed to the symmetric and asymmetric O-H stretching modes, respectively. However, only asymmetric O-H stretching mode is observed in the 21KOTF, which can be attributed to the decrease of free water. When 1 and 3 m DHA were added into the 21KOTF, the peak intensity of the symmetric O-H stretching mode is strengthened again, implying that the addition of DHA makes the O-H stretching vibration tend to convert to states of the low concentration solution, indicating the freedom of water is enhanced[35]. Therefore, the above NMR and Raman results certify the interaction between DHA and K^+, and the DHA could weaken the electronic density of H_2O in the modified K^+ solvation shell.

The solvation structures of K^+ in the 21KOTF and 21KOTF-1DHA are further analyzed by ab initio molecular dynamics (AIMD) simulations, the simulated solvation structures and corresponding radial distribution functions (RDFs) of K^+ with O-atom are shown in Fig. 2c–f[36]. The primary solvation shell (PSS) of K^+ in the 21KOTF solution is composed of H_2O molecules and OTF^- anions, and the bond lengths of K-O_{water} and K-O_{OTF} are both around 2.7 Å. By contrast, the addition of 1 m DHA leads to a conspicuous change in the PSS of K^+, where DHA coordinates with K^+ to form K^+-DHA and the peak of K-O_{DHA} still locates at around 2.7 Å. The AIMD simulation results suggest that the solvation structures in the 21KOTF electrolyte are mainly present in K^+-H_2O, while K^+-DHA species exist in the 21KOTF-1DHA electrolyte. Moreover, the higher binding energy of K^+-DHA than K^+-H_2O reveals that K^+ is more favorable to interact with DHA than with H_2O.

Interaction between the intercalated cations and the interstitial water

To establish the storage mechanism of MnHCC, Fourier transform infrared (FTIR) spectroscopy measurements were carried out to reveal the chemical bonding inside the MnHCC electrode at different states of charge (SOC). As shown in Fig. 3a, peaks of the interstitial water located at around 1605 cm^{-1} are significantly weakened during the discharging–charging processes in the 21KOTF electrolyte[20], which likely results from the dehydration of the MnHCC electrode due to the coordination of interstitial water with K^+-H_2O. By contrast, the peak intensity of the interstitial water of the electrode remains strong in the 21KOTF-1DHA electrolyte after the fully charged process (Fig. 3b) due to the self-shielding effect of the intercalated K^+-DHA. The broad peaks appearing at around 1570 cm^{-1} could be ascribed to the intercalated K^+-DHA[37]. Along with the potassiation process of the electrodes, the Mn-N ≡ C-Cr^{III} peaks (2157 cm^{-1}) gradually become weak and the peak of Mn-N ≡ C-Cr^{II} bonding (2129 cm^{-1}) appears. The charging process reverses the above process, which suggests the redox reaction of the $Cr^{III/II}$ is reversible. Notably, after 300 cycles, while the MnHCC electrodes tested in the 21KOTF/-1DHA electrolytes maintain their cubic phase, marked disparities emerge in the FTIR peak intensities corresponding to interstitial water content. These findings provide compelling evidence for the efficacy of the cation-self-shielding strategy (Supplementary Fig. 26). The ex situ X-ray photoelectron spectra (XPS) measurements and the cryo-scanning transmission electron microscopy (cryo-STEM) line scan of the fully discharged MnHCC electrode further confirm the redox reaction of MnHCC and intercalation of DHA (Supplementary Figs. 27–31 and related discussions)[38,39].

To quantitatively analyze the de-/potassiation processes of MnHCC, *operando* electrochemical quartz crystal microbalance (EQCM) was employed to explore the de-/intercalation charge carriers in MnHCC. Figure 3c, e and d, f demonstrate the CV curves and the corresponding mass changes of the MnHCC negative electrodes in the 21KOTF and 21KOTF-1DHA electrolytes during the redox processes, respectively. Regarding the reduction process in 21KOTF, the slope of the black dot curve was calculated to be 58 g per mole charge, which represents that the mole weight of the average intercalation cations is equivalent to K^+-H_2O. Instead, the oxidation process divides the line into two parts with the slope of 76 and 58 g per mole charge, indicating a mixture of K^+-$2H_2O$ and K^+-H_2O de-intercalate from the electrode structure. The one more captured H_2O by K^+ is from the interstitial water of MnHCC to a large extent, resulting in enhanced ion-diffusion barriers of the electrode, which needs a high-potential plateau to overcome for subsequent de-intercalation of the K^+-H_2O ions. In the 21KOTF-1DHA electrolyte, the mole weights of the de-/intercalation charge carriers are almost the same, representing K^+-0.5DHA, which suggests that the interstitial water has been repelled and remains in the electrode structure. The EQCM results further verify the above-postulated storage mechanisms of the MnHCC electrode in the two electrolytes.

AIMD simulations were further employed to illustrate the kinetics of the coordination of K^+-H_2O and K^+-DHA in the MnHCC skeletons. As shown in Fig. 3g, the simulated structure demonstrates that after K^+-H_2O enters the MnHCC electrode, the K^+ ion will form a saturated solvation shell by bonding with 5 H_2O molecules in the water-rich structure (K^+-$5H_2O$). During the de-intercalation process, the charge carriers should be K^+-H_2O or K^+-$2H_2O$ based on the above EQCM results, thus no less than three K-O bonds tend to disconnect from K^+-$5H_2O$ ions. By contrast, K^+-2DHA-$3H_2O$ will be formed in the MnHCC electrode during discharging process, where two K-O bonds with DHA and three with interstitial H_2O are calculated (Fig. 3h). Considering the de-solvation effect, all the three bonded H_2O molecules would remain in the structure during the charging process, that is, the K^+-DHA could prevent the dehydration process significantly. The AIMD simulations not only further support the results of EQCM, but also clarify the coordination and de-solvation process of the interstitial water of MnHCC in two different electrolytes.

AIMD simulations were also performed to investigate the migration processes of K^+ in the MnHCC electrode structure hosting K^+-H_2O and K^+-DHA. As shown in Fig. 3i, mean square displacement (MSD) curves exhibit the diffusion coefficients of various elements in the MnHCC electrode hosting K^+-H_2O. As the K^+ migrates, the O3, O6, O13, and O17, which coordinate with K^+, also migrate significantly. However, the O2, O12, O15, and O16, which form K-O bonds with K^+ initially (Supplementary Fig. 32a), demonstrate negligible migration, which implies the bonding and de-bonding behavior between the K^+ and different interstitial water molecules during the migration process (Supplementary Fig. 32b, c). By contrast, for the MnHCC electrode hosting K^+-DHA, we need to pay more attention to the migration process of DHA. As shown in Fig. 3j and Supplementary Fig. 32d–f, the O-atoms from DHA bond to K^+ during the whole migration process of the K^+, and the C19-21 (that comes from DHA) only engender slight migration. The process is similar to the movement of a satellite, that is, K^+ migrates around DHA. Figure 3k, l illustrates the different migration processes. Although the diffusion coefficient of DHA is low, those of the K^+ ions from K^+-H_2O and K^+-DHA are in the same order of magnitude.

Structural evolutions of MnHCC during the de-/potassiation processes

The in situ XRD analysis was carried out to monitor the structural evolution of MnHCC electrode during the charging–discharging processes in both 21KOTF and 21KOTF-1DHA electrolytes and the

https://doi.org/10.1038/s41467-025-59980-z

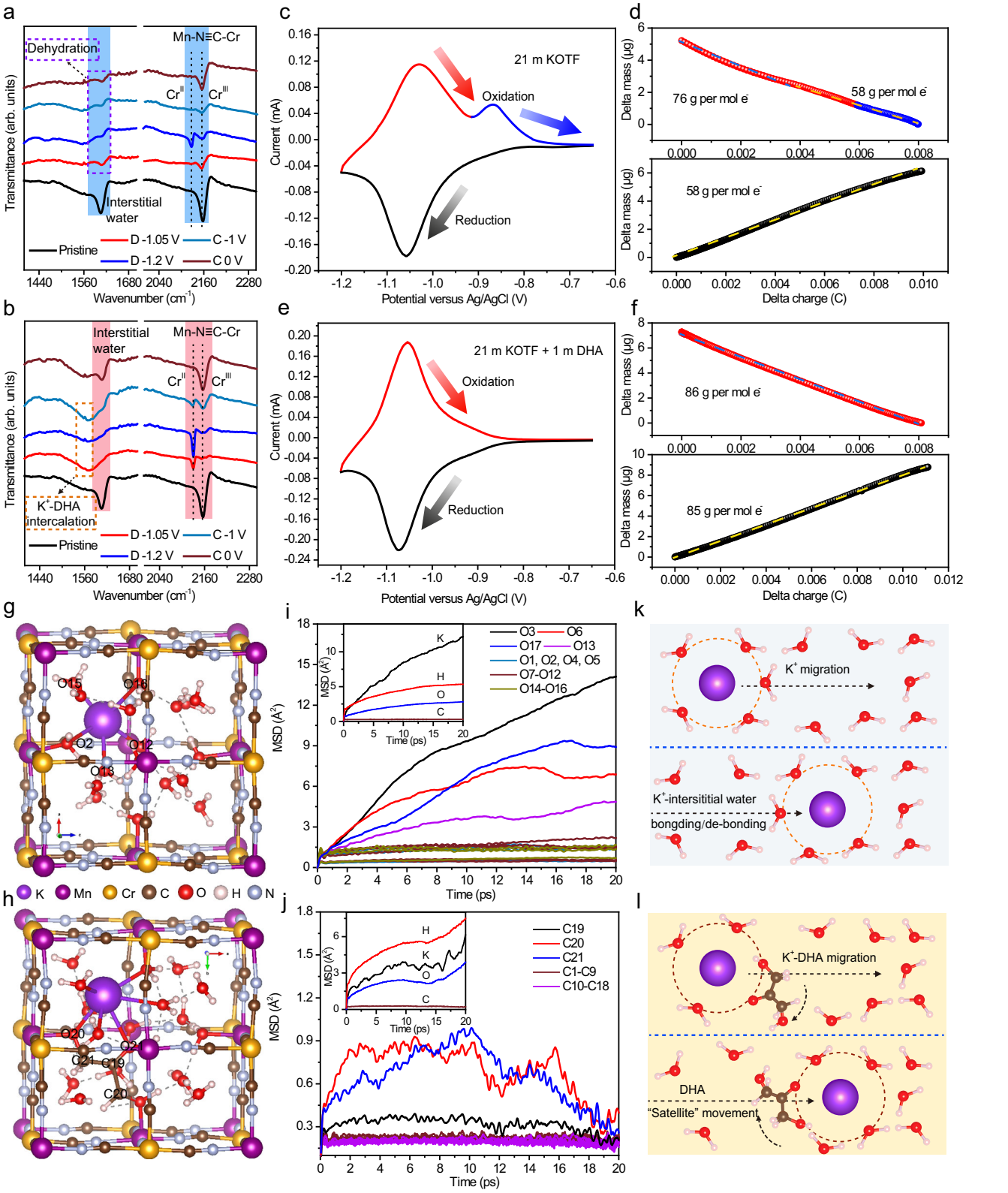

Fig. 3 | The de-/intercalation and migration of charge carriers. FTIR spectra of the MnHCC electrodes in the 21KOTF (**a**) and 21KOTF-1DHA (**b**) electrolytes at different states of charge with different shadowed areas representing different peaks. CV curves and the corresponding EQCM mass change profiles (top for oxidation and bottom for reduction) of the MnHCC electrodes in the 21KOTF (**c**, **d**) and 21KOTF-1DHA (**e**, **f**) electrolytes at a scan rate of 1 mV s^{-1}, respectively. Both CV curves are of the 2nd cycle. The optimal configurations of the MnHCC electrodes hosting K^+-H_2O (**g**) and K^+-DHA (**h**). **i** Mean square displacement (MSD) curves for various O-atoms in the MnHCC electrode hosting K^+-H_2O, the inset is the average MSD curves for K, H, O, and C elements. **j** MSD curves for various C-atoms in the MnHCC electrode hosting K^+-DHA, the inset is the average MSD curves for K, H, O, and C elements. Schematic migration processes of K^+-H_2O (**k**) and K^+-DHA (**l**) in the MnHCC electrodes.

https://doi.org/10.1038/s41467-025-59980-z

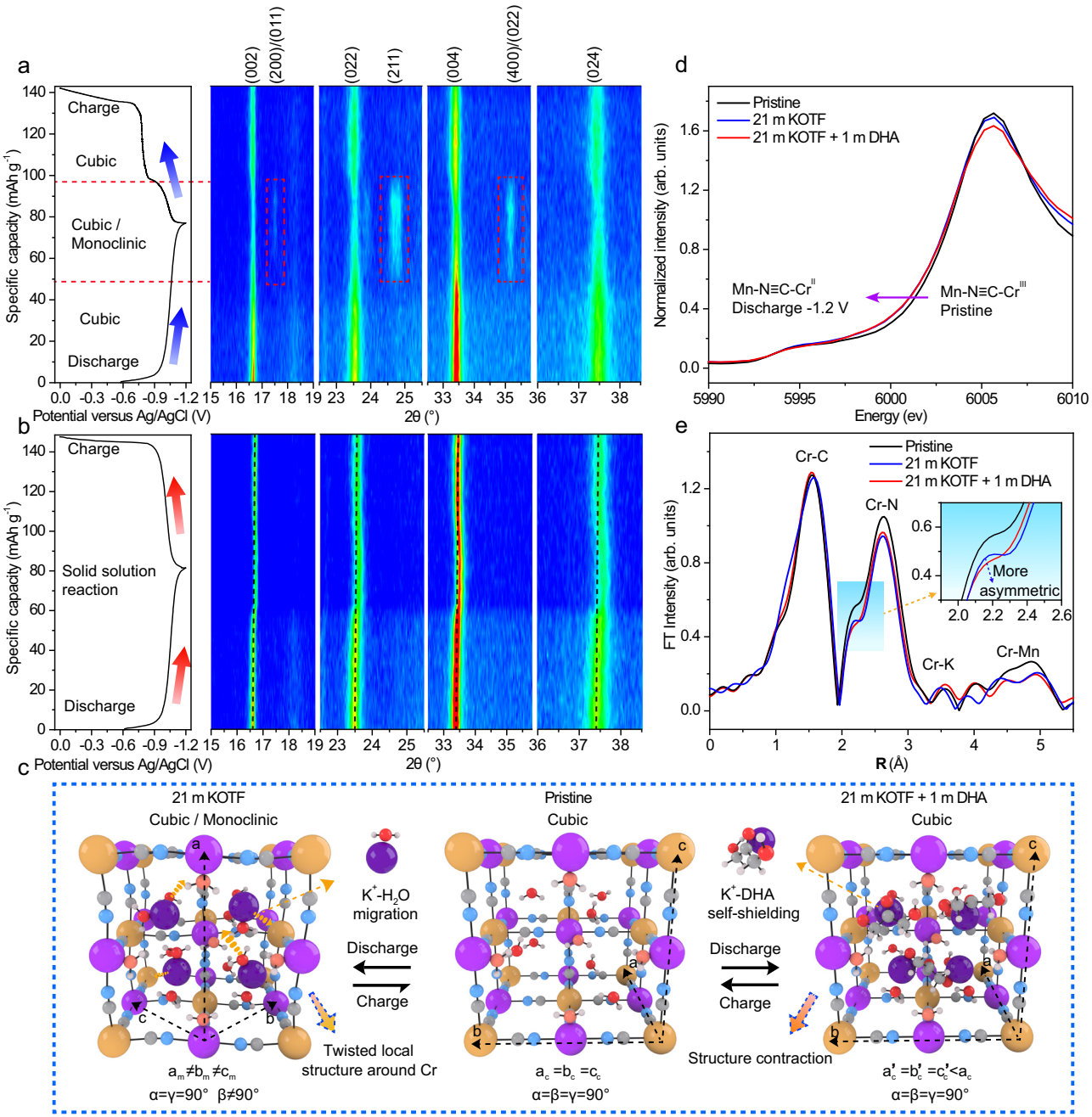

Fig. 4 | Structural evolutions of the MnHCC electrodes. 2D contour plots of in situ XRD patterns of the MnHCC electrodes for the first cycle in the 21KOTF (**a**) and 21KOTF-1DHA (**b**) electrolytes. **c** Schematic structural evolutions of the fully discharged MnHCC electrodes in the 21KOTF and 21KOTF-1DHA electrolytes. XANES (**d**) and EXAFS (**e**) spectra of the pristine and fully discharged MnHCC electrodes for the Cr K-edge in the 21KOTF and 21KOTF-1DHA electrolytes. The shadowed area represents the magnified area.

two-dimensional (2D) contour plots and curves are shown in Fig. 4a, b and Supplementary Fig. 33a, b, respectively. It can be seen clearly that MnHCC undergoes a phase transition between cubic and monoclinic phases in 21KOTF while experiencing a solid solution process in 21KOTF-1DHA. Note that no extra phase appears during the high charging potential, which further verifies the high charging plateau has nothing to do with the phase transition. Moreover, the distortion of the cubic structure can be attributed to the intensified electrostatic interactions between intercalated K^+-H_2O and electrode, and the absence of interstitial water aggravates the distortion of the cubic structure. We also conducted the ex situ XRD testing on the fully discharged MnHCC electrode in the 21KOTF electrolyte and fully charged MnHCC electrode in the 21KOTF/-1DHA electrolytes to figure out the details of the positions and the coordination environment of K and O atoms as well the percentage of the coexisting two phases (Supplementary Figs. 34–36, Supplementary Tables 5–7, and related discussions). On the contrary, the intercalated K^+-DHA cations could not only alleviate the de-intercalation of the interstitial water but also sustain the electrode structure. The detailed lattice parameters along the a-axis of MnHCC are examined by fitting the in situ XRD data (Supplementary Fig. 33), where the decrease of the lattice parameter of the MnHCC electrode in 21KOTF-1DHA is only about 0.039 Å at the fully discharged state. The structural evolutions of the discharged MnHCC electrodes in 21KOTF and 21KOTF-1DHA electrolytes are illustrated in Fig. 4c. The above in situ XRD results prove that the 21KOTF-1DHA electrolyte

https://doi.org/10.1038/s41467-025-59980-z

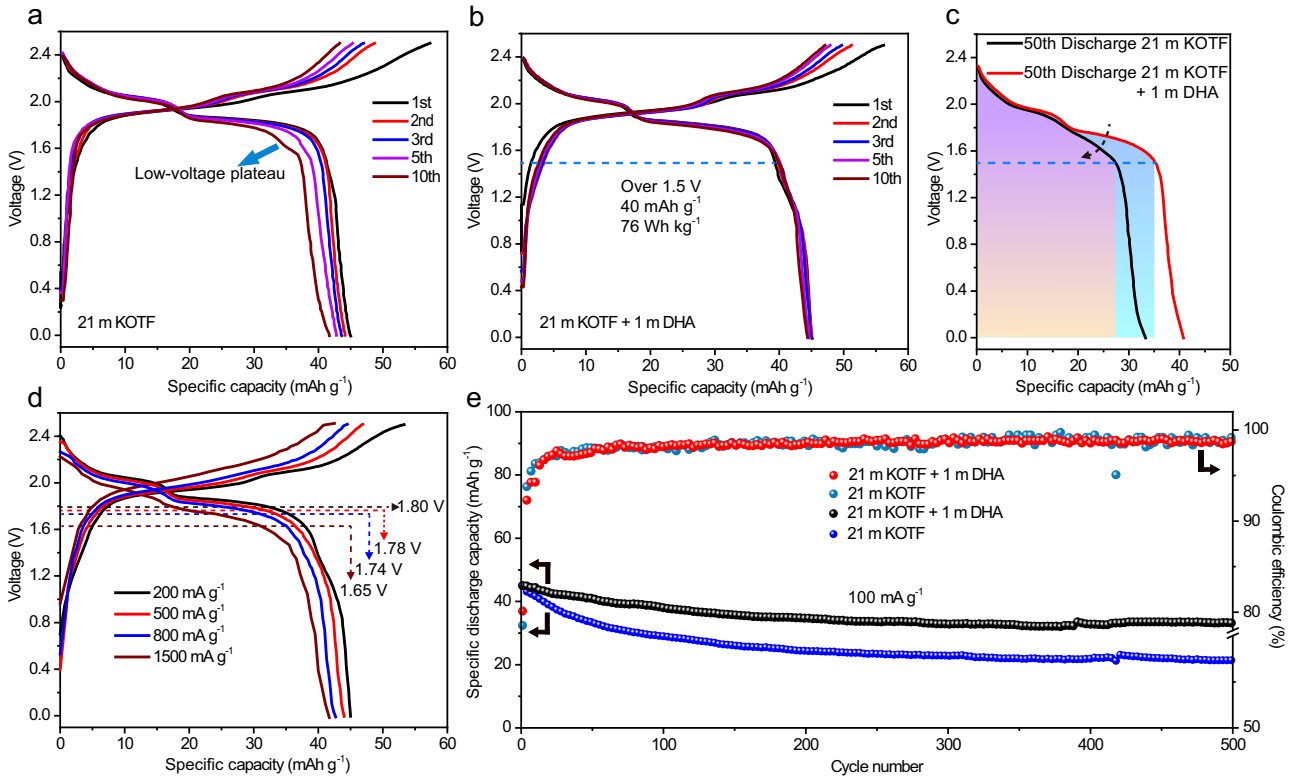

Fig. 5 | Electrochemical performance of all-PBA-based full cells. GCD curves of the MnHCC|21KOTF|KFeMnHCF-28 (**a**) and MnHCC|21KOTF-1DHA|KFeMnHCF-28 (**b**) full cells at 100 mA g^{-1}. **c** The 50th discharging curves of the MnHCC | | KFeMnHCF-28 full cells at 100 mA g^{-1} with 21KOTF (black curve) and 21KOTF-1DHA (red curve) as the electrolytes. Even after 50 cycles, the 21KOTF-1DHA electrolyte can still stabilize the discharging plateaus at high voltage. The shadowed areas represent the specific energy. **d** GCD curves of the MnHCC|21KOTF-1DHA|KFeMnHCF-28 full cell at different current rates. The average discharging voltages are marked with dashed lines. **e** Cycling performance of the MnHCC | |KFeMnHCF-28 full cells in the 21KOTF and 21KOTF-1DHA electrolytes at 100 mA g^{-1}. The electrochemical properties were evaluated using two-electrode cells at 27 °C, where the mass loading is around 30 mg cm^{-2} for the negative electrode and 15 mg cm^{-2} for the positive electrode, with equal electrode areas.

can improve the structural stability of the electrode during the charging-discharging processes.

The valence and local structural changes of the MnHCC electrode during the potassiation process were further investigated by using X-ray absorption spectroscopy (XAS). As shown in Fig. 4d, the normalized Cr K-edge X-ray absorption near-edge structure (XANES) spectra of fully discharged electrodes in different electrolytes illustrate the reduction of Cr^{III} due to the left-shift of the edges compared with the pristine sample[40]. More importantly, Fourier-transform (FT) magnitudes of the Cr K-edge extended X-ray absorption fine structure (EXAFS) spectra were utilized to analyze the local structural changes of the electrodes (Fig. 4e), besides we also fitted the Cr K-edge EXAFS and the corresponding *k*-space of the pristine and the fully discharged MnHCC electrodes (Supplementary Fig. 37 and Supplementary Table 8). The Cr-C and Cr-N peaks are related to the local absence of $Cr(CN)_6$. Compared to the pristine electrode, the fully discharged electrode in the 21KOTF electrolyte demonstrates different peak shapes of Cr-C and Cr-N shells, a new peak even occurs at the left of the Cr-N peak, which suggests the distorted local structure around Cr due to the intercalated K^+-H_2O[41]. Furthermore, the negative shift of the Cr-K signal can be attributed to the constricted structure. However, regarding the fully discharged electrode in the 21KOTF-1DHA electrolyte, the peaks demonstrate nil symmetry and position changes compared with the pristine electrode, which indicates DHA can alleviate the distortion of the electrode structure during the potassiation process.

All-PBA-based full AKIBs

To evaluate the practical application prospect of the MnHCC negative electrode and 21KOTF-1DHA electrolyte, we assembled all-PBA-based full AKIBs with the high-temperature dried Fe-substituted MnFe-based PBA as the positive electrode (MnHCC|21KOTF-1DHA|KFeMnHCF-28). The XRD[5], ICP, and thermal gravimetric analysis (TGA) measurements were conducted to verify the monoclinic phase of the positive electrode, and the stoichiometric composition can be determined to be $K_{1.97}Fe_{0.2}Mn_{0.8}[Fe(CN)_6]_{0.97}{\cdot}0.38H_2O$ (Supplementary Figs. 38 and 39 and Supplementary Table 9). The GCD curves and cycling performance further verify the suitability and compatibility of KFeMnHCF-28 with an average initial reversible capacity of 132.1 mAh g^{-1} in the 21KOTF-1DHA electrolyte (Supplementary Figs. 40 and 41, and related discussions). As shown in Fig. 5a, the GCD curves of the full cell with 21KOTF electrolyte show a severe degeneration of the capacity, and the low-voltage plateau also suffers a gradual decrease. By contrast, the full cell with 21KOTF-1DHA electrolyte delivers improved capacity retention and negligible degradation of the discharging plateaus (Fig. 5b, c), which are located at around 2.1 V and 1.8 V. Based on the mass of both negative and positive electrodes, the full cell demonstrates the specific energy of around 82 Wh kg^{-1}, more than 92% of which comes from the voltage above 1.5 V, which is among the highest specific energy at high voltage for full AKIBs. The initial reversible capacity of 45 mAh g^{-1} is slightly affected by the capacitive behavior of the positive electrode side and the utilization of the discharge capacity over 1.5 V is independent of the capacitive effect below 1.5 V (Supplementary Fig. 42). Notably, the full cell can still deliver a high average discharging voltage of 1.65 V at the current rate of 1500 mA g^{-1} (Fig. 5d). Besides, the full AKIBs also exhibit 77% capacity retention at 100 mA g^{-1} over 500 cycles in the 21KOTF-1DHA electrolyte (Fig. 5e). We further compare the electrochemical performance of the assembled full cell with the previous reported ANIBs and AKIBs[5,6,17,18,21,33,42–49], and our full cell delivers

https://doi.org/10.1038/s41467-025-59980-z

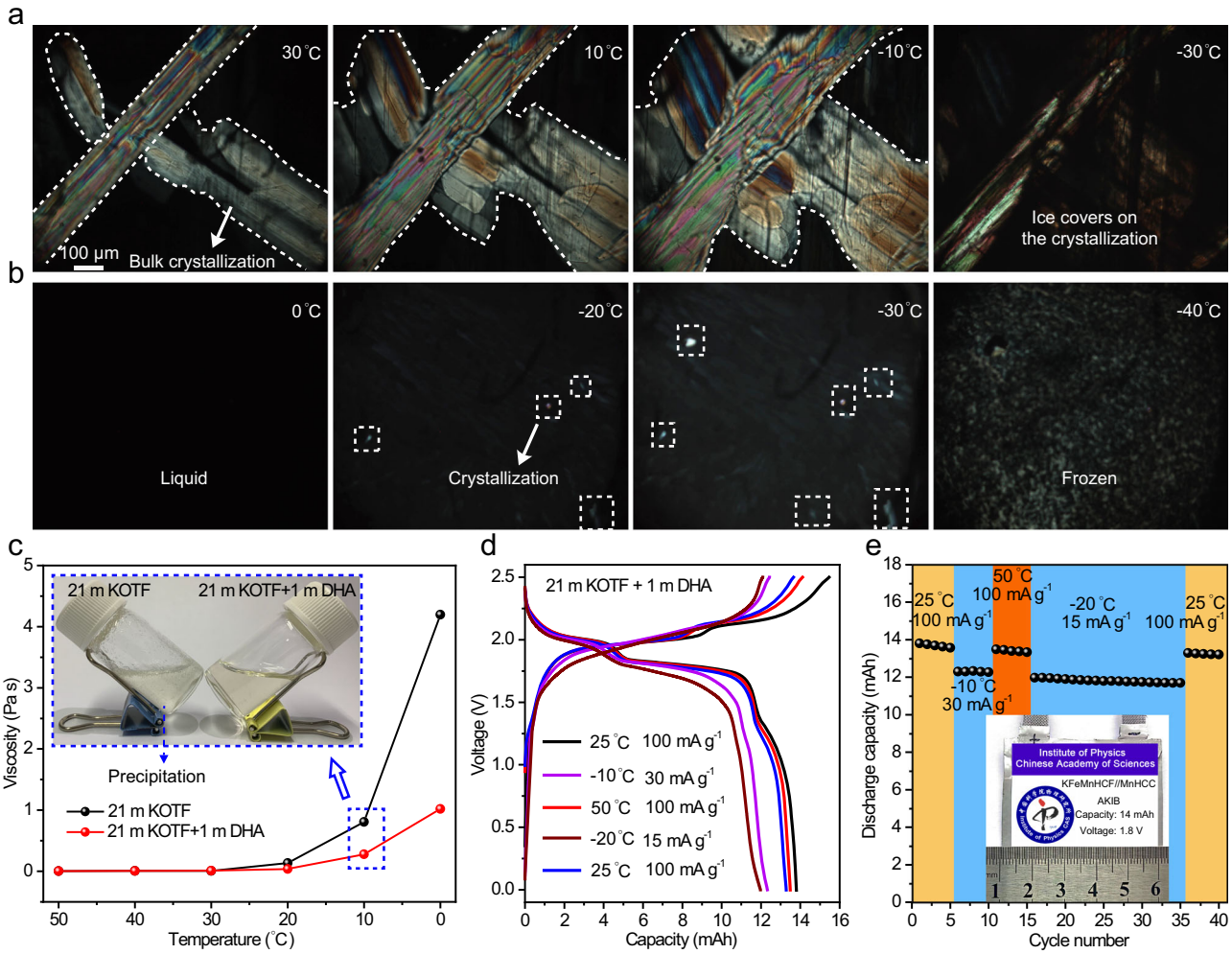

Fig. 6 | Properties of electrolytes and electrochemical performance of pouch cell at different temperatures. Polarizing microscope observation of the 21KOTF (**a**) and 21KOTF-1DHA (**b**) electrolytes at different temperatures. **c** Viscosity at different temperatures for the 21KOTF and 21KOTF-1DHA electrolytes. The inset in (**c**) is the digital image of the electrolytes at 10 °C. Electrochemical performance of the MnHCC|21KOTF-1DHA|KFeMnHCF-28 pouch cell at different current rates and temperatures from 0 V to 2.5 V for the GCD curves (**d**) and the cycling performance (**e**). The inset in (**e**) is the digital image of the assembled pouch cell. The mass loading is around 40 mg cm^{-2} for the negative electrode and 20 mg cm^{-2} for the positive electrode, with equal electrode areas.

superior average discharging voltage and specific energy as well capacity above 1.5 V (Supplementary Fig. 43, corresponding detailed parameters are listed in Supplementary Table 10).

Moreover, we also investigated if the modified electrolyte could support the low-temperature operation of the batteries, and the 21KOTF-1DHA electrolyte demonstrates a lower freezing temperature (−44 °C) than that of the 21KOTF electrolyte (−34 °C, Supplementary Fig. 44). Notably, the in situ polarizing microscope images show that bulk crystallization could be observed in the 21KOTF electrolyte even above 30 °C, while the DHA additive enables to suppress the precipitation of the modified electrolyte until −30 °C, which can be attributed to the strong chemical coordination between K^+ and DHA (Fig.6a, b) and correlates to the improved viscosity as well conductivity of the 21KOTF-1DHA electrolyte at different temperatures (Fig. 6c and Supplementary Fig. 45). Furthermore, the GCD and cycling performance of a 14 mAh pouch cell at different rates (100, 30, and 15 mA g^{-1}) in a wide temperature range (−20 °C to 50 °C) was conducted in the 21KOTF-1DHA electrolyte. As shown in Fig. 6d, e, the pouch cell could deliver a discharging capacity of around 14 mAh at 25 °C (100 mA g^{-1}) with the average discharging voltage of 1.8 V and can still maintain the capacity of 12 mAh at −20 °C (15 mA g^{-1}) with two discharging plateaus at around 2 and 1.74 V. After the pouch cell operates at low temperature for 20 cycles, we increased the temperature to 25 °C and 50 °C (100 mA g^{-1}), and the two plateaus climb back to around 2.1 and 1.8 V, thus, suggesting the good stability at low temperature and the resilience along with the temperature changes of the 21KOTF-1DHA electrolyte.

Discussion

In summary, we have highlighted the significant effect of interstitial water in improving the kinetics of PBA negative electrodes with the developed water-rich $K_{0.01}Mn[Cr(CN)_6]_{0.74}\cdot 4.75H_2O$ PBA negative electrode in AKIBs as a demo. It is found that the split charging plateaus originate from the dehydration process of interstitial water in the framework structure, resulting in deteriorated kinetics and large polarization. Comprehensive characterizations and AIMD simulations have been employed to quantitatively track and demonstrate the migration and de-intercalation processes of the interstitial water during de-potassiation. The cation-self-shielding strategy is then proposed to solve the issue by employing DHA as an indispensable electrolyte additive to coordinate with K^+. The newly formed self-shielding K^+-DHA cations could alleviate the interactions between K^+ and H_2O, repel the interstitial water in the structure, and maintain the average charging potentials, stabilizing the kinetics and structure of MnHCC. Meanwhile, the investigation of ZnHCC further verifies the dehydration problem and the cation-self-shielding strategy. Our ongoing project

showed that interstitial water also plays a critical role in PBA positive electrodes. As a result, the fabricated all-PBA-based MnHCC|21KOTF-1DHA|KFeMnHCF-28 full cell delivers an impressively high average discharging voltage of 1.82 V with around 76 Wh kg^{-1} practical specific energy coming from the voltage above 1.5 V, which is among the highest specific energy at high voltage for full AKIBs to date. This study not only redefines the critical role of the interstitial water in the PBA negative electrode to facilitate kinetics but also proposes a strategy to develop all-PBA-based AKIBs with the majority of specific energy maintained at the high-voltage plateaus, offering a potential avenue for the development of rich-water-containing electrodes and high-voltage aqueous rechargeable batteries for energy storage.

Methods

Materials synthesis

The MnHCC negative electrode was prepared by a simple co-precipitation method. Typically, 10 mL of 0.15 M manganese chloride ($MnCl_2$, 99%, Alfa) aqueous solution was dropped into 10 mL 0.15 M potassium hexacyanochromate ($K_3Cr(CN)_6$, 99.99%, Sigma-Aldrich) aqueous solution and mixed for 24 h with magnetic stirring. The solution was centrifuged, and the precipitate was washed with deionized water and ethanol (>99%, Sinopharm Chemical Reagent) mixture solvent before being dried at room temperature. Finally, the green colored MnHCC product was obtained. For comparison, the MnHCC sample dried at 100 °C under vacuum was also prepared. The ZnHCC was prepared with the same process, but $MnCl_2$ was replaced by Zinc chloride ($ZnCl_2$, anhydrous, >98%, Alfa). The KFeMnHCF-28 positive electrode was prepared by a similar method. About 1.267 g potassium ferrocyanide trihydrate ($K_4Fe(CN)_6{\cdot}3H_2O$, 98.5%, Alfa) was added to 70 mL of deionized water (30 mL) and EG (40 mL, 99%, Alfa) mixture solvent to form solution A. Then 0.1668 g iron sulfate heptahydrate ($FeSO_4{\cdot}7H_2O$, 99+%, Acros) and 0.4066 g manganese sulfate monohydrate ($MnSO_4{\cdot}H_2O$, 99+%, Acros) were added to 40 mL of deionized water (20 mL) and EG (20 mL) mixture solvent to form solution B. Solution B was added into solution A and mixed for 12 h with stirring. The obtained mixture solution was centrifuged before being dried at 170 °C under vacuum. Finally, the light blue-colored KFeMnHCF-28 positive electrode material was obtained. The KFeMnHCF-19 and KFeMnHCF-3565 could be prepared by the same method.

Electrochemical measurements

The electrodes were free-standing films, which were composed of the active materials, carbon nanotubes (CNTs, 98%, Kerui Nano (Guangdong)) conducting carbon, and polytetrafluoroethylene (PTFE, 60 wt% PTFE dispersion, Hefei Kejing Materials Technology) binder with a mass ratio of 7:2:1. The components were mixed in a mortar and ground for 30 min. With ethanol as a processing aid, the electrode slurries were continuously rolled into free-standing films using a stainless-steel rod in air at room temperature. Finally, the negative electrodes were dried at room temperature, whereas the positive electrodes were dried at 100 °C. The mass loading of negative and positive electrodes are around 30 mg cm^{-2} (7 × 7 mm^2) and 15 mg cm^{-2} (7 × 7 mm^2), respectively, unless mentioned otherwise. We characterized the independent electrochemical performance of the MnHCC, ZnHCC negative electrodes, and KFeMnHCF-28 positive electrode in three-electrode Swagelok® cells, where either of them serve as the working electrodes, Ag/AgCl serves as the reference electrode (E = 0.210 V versus SHE, the calibration was performed by freshly prepared saturated KCl (>99.8%, Sinopharm Chemical Reagent) solutions before the three-electrode cells testing, R1038, GAOSSUNION), and an active carbon (>99%, Fuzhou Yihuan Carbon) free-standing film serves as the counter electrode (8 × 8 mm^2). 1 m KOTF (>98%, Tci), 21 m KOTF + X m DHA (X = 0, 0.5, 1, 2, 3, >97.2%, Tci) and 21 m KOTF + 1 m glucose (99%, Innochem)/EG/glycerol (99.6%, Innochem)/acetone (99+%, Acros) aqueous solutions were used as the electrolytes in this study (~400 µL for the three-electrode cells and ~200 µL for the two-electrode cells). For the full cells using Swagelok® cells, the mass ratio of MnHCC: KFeMnHCF-28 is 2:1. For the pouch cell, the mass loading of the MnHCC negative electrode and KFeMnHCF-28 positive electrode are 40 and 20 mg cm^{-2}, respectively. The employed separators are glass fibers (Whatman GF/F, d = 12 mm). Notably, all the KFeMnHCF-28 electrodes used in this study are consistent. The GCD measurements were carried out using a LAND CT2001A battery tester, and the CV tests were performed on a CHI760e electrochemical workstation. We measured electrochemical impedance spectroscopy (EIS) with an electrochemical workstation (IM6e Zahner). The EIS measurements were performed in the frequency range from 1 MHz to 0.1 Hz with an applied amplitude of 10 mV, potentiostatic signal, and 10 points per decade during each measurement. The open-circuit voltage time applied before carrying out the EIS measurement at the desired SOC is 10 min. DRT was conducted by the MATLAB GUI toolbox developed by Ciucci's research team[50]. All the batteries operated at 27 °C, and the potential is not iR-corrected in the three-electrode cells, unless mentioned otherwise. The single electrochemical data was collected from at least three cells. The consistent efficacy of the cation-self-shielding strategy resulted in highly reproducible electrochemical behaviors; therefore, statistical analysis results are not shown.

CV curves of the MnHCC electrode at various scan rates between 0 and −1.2 V were conducted, and the peak currents have a linear relationship to the square root of the scan rates ($v^{1/2}$). This indicates that the charging/discharging process is diffusion-controlled and the apparent diffusion coefficient can be estimated according to the Randles–Sevcik equation as:

$$i_p = (2.69\text{x}10^5)n^{3/2}AD^{1/2}Cv^{1/2} \quad (1)$$

where i_p represents the peak current, n is the number of electrons per molecule during the reaction, A represents the effective contact area between the electrolyte and electrode, D is the apparent diffusion coefficient of charge carriers, and C is the concentration of charge carriers in the electrode.

For further understanding of the kinetics during the diffusion process of charge carriers, GITT was measured at a current rate of 300 mA g^{-1} with the repeated current pulses of 60 s (discharge) and 35 s (charge), and the open-circuit resting time of 15 min (discharge) and 10 min (charge). The apparent diffusion coefficients of K^+-H_2O and K^+-DHA ions inside the MnHCC electrode can be calculated by the following equation:

$$D = \frac{4}{\pi\tau}\left(\frac{m_B V_M}{M_B S}\right)^2\left(\frac{\Delta E_S}{\Delta E_\tau}\right)^2\left(\tau \ll \frac{L^2}{D}\right) \quad (2)$$

where M_B and V_M are the molecular weight and molar volume of the MnHCC electrode, m_B, S, and L are the mass, the active surface area, and the thickness of the electrode, respectively. τ is the current duration time, ΔE_τ and ΔE_S represent different potential changes during the current pulse and in the steady-state voltage during the step at the plateau potential, respectively.

Material characterization

The chemical composition of the obtained negative electrode material was confirmed by ICP-AES (Agilent 5110), and TGA (Rigaku TG/DTA8122). The morphology and structure were characterized by using the SEM (Hitachi-S4800) and X'Pert Pro MPD XRD (D8 Bruker) with Cu Kα radiation (λ = 1.5405 Å). In situ XRD, ex situ XPS (ESCALAB 250 Xi, ThermoFisher with Mg/Al Kα radiation), and FTIR (Nicolet FTIR Is 10) were employed to analyze the crystal structures, electronic structures, and chemical composition changes of the electrode during the charging–discharging processes. Cryo-scanning transmission electron microscopy (cryo-STEM) line scan and corresponding energy-

dispersive X-ray spectroscopy were carried out using an aberration-corrected microscope (JEOL JEM-ARM200F) under cryogenic temperatures (−180 °C) at 200 kV. X-ray absorption spectroscopy was performed on the 1W1B beamline of the Beijing Synchrotron Radiation Facility (BSRF, Beijing, China), containing XANES and EXAFS measurements. The spectra were analyzed with the ATHENA program[51]. After electrodes were removed from testing cells, residual electrolyte on electrodes is completely removed by rinsing with propylene carbonate (PC, >98%, Aladdin), and dimethyl carbonate (DMC, >98%, Aladdin) thoroughly and the thick electrode films would be pressed and rolled again. Note that KOTF has a large solubility in PC, and DMC can facilitate the evaporation process. The chemical environment of the electrolyte was analyzed by nuclear magnetic resonance (NMR, Bruker DRX 500 spectrometer), and Raman (NRS-5100 spectrometer (JASCO)). The DSC was carried out in DSC200F3, and the polarizing microscope was characterized on Olympus BX51TRF.

EQCM experiments

Operando EQCM was performed on a QCM200 quartz crystal microbalance. The electrode slurry was prepared by mixing 7 mg of active materials, 2 mg of CNTs, and 6 mg of polyvinylidene fluoride (PVdF) in 420 µL NMP, where it was dried at room temperature on the quartz crystal disk (O100RX3, p/n 6-615 Ti/Au, 5 MHZ). The frequency change (Δf) was conducted during CV tests, and converted into the mass change (Δm) of the electrode by Sauerbrey's equation:

$$\Delta m = \frac{A\sqrt{\mu_Q \rho_Q}}{2f_0^2}\Delta f = -C_f \Delta f \tag{3}$$

where A is the piezoelectrical electrode area, μ_Q is the shear modulus of quartz ($2.947 \times 10^{11}\,g\,cm^{-1}\,s^{-2}$), ρ_Q is the density of quartz ($2.649\,g\,cm^{-3}$), f_0 is the fundamental resonance frequency of the quartz, C_f, Δm, and Δf are the sensitivity factor, mass change, and frequency change, respectively. C_f can be obtained by calculating the relation based on mass change and frequency between the coated electrodes and the clean, uncoated quartz. The value of the calibration constant used in this work is 33 ng Hz^{-1}, and the exchanged molecular weight of the ion (M_w) was calculated by the following equation:

$$M_W = \frac{\Delta m\, n\, F}{\Delta Q} \tag{4}$$

where F, n, and ΔQ are the Faraday constant (96,485 C mol^{-1}), valence number of ions, and charge quantity passed through the electrode in Coulombs, respectively.

Computation

To simulate the solvation structure of K^+ in the 21KOTF and 21KOTF-1DHA solutions, two calculation models were built according to the mol ratio among different molecules. The first model consists of 10 KOTF and 27 H_2O molecules, and the second model consists of 10 KOTF, 27 H_2O, and 1 DHA molecule. The initial position of each molecule is distributed in a cubic box randomly and homogeneously. A series of volume relaxation, in which the size of the simulation box is isotropically scaled, is carried out to look for the lattice with the lowest total energy. The selected lattice is determined as the initial configuration used for the following AIMD simulations. In this way, the lattice lengths determined for models 1 and 2 are 14.963 and 15.198 Å, respectively. The AIMD simulations for the two models were performed at two temperatures, including 300 and 500 K. The pair radial distribution function (PRDF) and the normalized radial distribution function ($g(r)$) are statistically obtained from the configurations that appeared in AIMD simulations.

To evaluate the strength of the DHA and H_2O molecules to bond with the K^+ ion, the configuration of K^+-DHA and K^+-H_2O is taken from the last structure obtained from AIMD. The energy and the charge density for both the single DHA, H_2O, K^+ unit and the bonded K^+-DHA, K^+-H_2O are calculated. The binding energy of K^+-DHA and K^+-H_2O, as well as the charge density difference, are estimated by using the values of the entirety to subtract the value of each constituent part.

To simulate the local structure and the migration properties of K^+ in the negative electrode, one K^+ ion, and 18 H_2O molecules were introduced into the MnHCC lattice. To understand the effect of the additive, one more DHA molecule is also put into the lattice for comparison. The models without and with DHA molecules are in the composition of $KMn_4[Cr(CN)_6]_3{\cdot}18H_2O$ and $KMn_4[Cr(CN)_6]_3{\cdot}18H_2O{\cdot}C_3O_3H_6$, respectively. The lattice parameters with the lowest total energy were determined in the same way as the simulations in the KOTF solutions. The AIMD simulations were performed on these two models at 300 K, and the K^+ ion diffusion was analyzed according to the MSDs.

The calculations were carried out with the Vienna ab initio simulation package[52]. The present data were obtained with a parameterized exchange-correlation functional according to Perdew-PBE[53]. The van der Waals interaction is corrected with DFT-D3[54,55]. For the static energy calculations, the cutoffs for the wave function and density are 520 and 780 eV, respectively. The energy convergence criterion is 10^{-5} eV. The AIMD simulations were carried out with the timestep of 1 fs for both the KOTF solutions and the K-MnHCC models. The simulations lasted for 30 ps for each model by a Nose thermostat. To keep the computational cost at a reasonable level, only the Gamma point is used for the Brillouin zone sampling in AIMD calculations. The PRDF and $g(r)$ are extracted from the last 10 thousand configurations (among 20–30 ps), and the MSDs are obtained from the configurations after 10 ps.

Data availability

The data supporting the findings of this study are available within the article and its Supplementary Information files. Source data are provided with this paper.

References

1. Wang, W. et al. Reversible structural evolution of sodium-rich rhombohedral Prussian blue for sodium-ion batteries. *Nat. Commun.* **11**, 980 (2020).
2. Hurlbutt, K., Wheeler, S., Capone, I. & Pasta, M. Prussian blue analogs as battery materials. *Joule* **2**, 1950–1960 (2018).
3. Liang, Z., Tian, F., Yang, G. & Wang, C. Enabling long-cycling aqueous sodium-ion batteries via Mn dissolution inhibition using sodium ferrocyanide electrolyte additive. *Nat. Commun.* **14**, 3591 (2023).
4. Su, D., McDonagh, A., Qiao, S. Z. & Wang, G. High-capacity aqueous potassium-ion batteries for large-scale energy storage. *Adv. Mater.* **29**, 1604007 (2017).
5. Jiang, L. et al. Building aqueous K-ion batteries for energy storage. *Nat. Energy* **4**, 495–503 (2019).
6. Ge, J., Fan, L., Rao, A. M., Zhou, J. & Lu, B. Surface-substituted Prussian blue analogue cathode for sustainable potassium-ion batteries. *Nat. Sustain.* **5**, 225–234 (2022).
7. Song, J. et al. Removal of interstitial H_2O in hexacyanometallates for a superior cathode of a sodium-ion battery. *J. Am. Chem. Soc.* **137**, 2658–2664 (2015).
8. Wu, J. et al. Modification of transition-metal redox by interstitial water in hexacyanometalate electrodes for sodium-ion batteries. *J. Am. Chem. Soc.* **139**, 18358–18364 (2017).
9. Choi, A. et al. Enhancing efficiency of low-grade heat harvesting by structural vibration entropy in thermally regenerative electrochemical cycles. *Adv. Mater.* **35**, 2303199 (2023).
10. Kim, D., Choi, A., Park, C., Kim, M.-H. & Lee, H.-W. Investigating the role of interstitial water molecules in copper hexacyanoferrate for

sodium-ion battery cathodes. *J. Mater. Chem. A* **11**, 13535–13542 (2023).
11. Shan, X. et al. Structural water and disordered structure promote aqueous sodium-ion energy storage in sodium-birnessite. *Nat. Commun.* **10**, 4975 (2019).
12. Nam, K. W. et al. The high performance of crystal water containing manganese birnessite cathodes for magnesium batteries. *Nano Lett.* **15**, 4071–4079 (2015).
13. Wu, X. et al. Diffusion-free Grotthuss topochemistry for high-rate and long-life proton batteries. *Nat. Energy* **4**, 123–130 (2019).
14. Charles, D. S. et al. Structural water engaged disordered vanadium oxide nanosheets for high capacity aqueous potassium-ion storage. *Nat. Commun.* **8**, 1–8 (2017).
15. Zhang, X. et al. Hydration enables air-stable and high-performance layered cathode materials for both organic and aqueous potassium-ion batteries. *Adv. Funct. Mater.* **32**, 2204318 (2022).
16. Pasta, M., Wessells, C. D., Huggins, R. A. & Cui, Y. A high-rate and long cycle life aqueous electrolyte battery for grid-scale energy storage. *Nat. Commun.* **3**, 1–7 (2012).
17. Chen, H. et al. Use of a water-in-salt electrolyte to avoid organic material dissolution and enhance the kinetics of aqueous potassium ion batteries. *Sustain. Energy Fuels* **4**, 128–131 (2020).
18. Li, Y. et al. An ultra-long life aqueous full K-ion battery. *J. Mater. Chem. A* **9**, 2822–2829 (2021).
19. Zhang, X. et al. Recent advances and perspectives in aqueous potassium-ion batteries. *Energy Environ. Sci.* **15**, 3750–3774 (2022).
20. Wheeler, S., Capone, I., Day, S., Tang, C. & Pasta, M. Low-potential Prussian blue analogues for sodium-ion batteries: manganese hexacyanochromate. *Chem. Mater.* **31**, 2619–2626 (2019).
21. Nakamoto, K., Sakamoto, R., Sawada, Y., Ito, M. & Okada, S. Over 2 V aqueous sodium-ion battery with Prussian blue-type electrodes. *Small Methods* **3**, 1800220 (2019).
22. Song, W. et al. Aqueous sodium-ion battery using a $Na_3V_2(PO_4)_3$ electrode. *ChemElectroChem* **1**, 871–876 (2014).
23. Wessells, C. D., Peddada, S. V., Huggins, R. A. & Cui, Y. Nickel hexacyanoferrate nanoparticle electrodes for aqueous sodium and potassium ion batteries. *Nano Lett.* **11**, 5421–5425 (2011).
24. Mullaliu, A., Asenbauer, J., Aquilanti, G., Passerini, S. & Giorgetti, M. Highlighting the reversible manganese electroactivity in Na-rich manganese hexacyanoferrate material for Li- and Na-ion storage. *Small Methods* **4**, 1900529 (2020).
25. Maisuradze, M. et al. Mapping heterogeneity of pristine and aged Li- and Na-Mnhcf cathode by synchrotron-based energy-dependent full field transmission X-ray microscopy. *Small Methods* **7**, 2300718 (2023).
26. Mullaliu, A., Aquilanti, G., Conti, P., Giorgetti, M. & Passerini, S. Effect of water and alkali-ion content on the structure of manganese (II) hexacyanoferrate (II) by a joint operando X-ray absorption spectroscopy and chemometric approach. *ChemSusChem* **13**, 608–615 (2020).
27. Zhao, S. et al. The rise of prussian blue analogs: challenges and opportunities for high-performance cathode materials in potassium-ion batteries. *Small Struct.* **2**, 2000054 (2021).
28. Sun, P. et al. Simultaneous regulation on solvation shell and electrode interface for dendrite-free Zn ion batteries achieved by a low-cost glucose additive. *Angew. Chem. Int. Ed.* **133**, 18395–18403 (2021).
29. Gui, Q., Li, Y. & Liu, J. Bendable quasi-solid-state aqueous sodium-ion batteries operated at -30 °C. *J. Colloid Interface Sci.* **662**, 119–128 (2024).
30. Pham, T. H., Lee, W.-H., Byun, J.-H. & Kim, J.-G. Improving the performance of primary aluminum-air batteries through suppressing water activity by hydrogen bond-rich glycerol solvent additive. *Energy Storage Mater.* **55**, 406–416 (2023).
31. Shi, X. et al. Metallic zinc anode working at 50 and 50 mAh cm^{-2} with high depth of discharge via electrical double layer reconstruction. *Adv. Funct. Mater.* **33**, 2211917 (2023).
32. Wang, T. et al. Simultaneous regulation on electrolyte structure and electrode interface with glucose additive for high-energy aluminum metal-air batteries. *Energy Storage Mater.* **53**, 371–380 (2022).
33. Jiang, L. et al. High-voltage aqueous Na-ion battery enabled by inert-cation-assisted water-in-salt electrolyte. *Adv. Mater.* **32**, 1904427 (2020).
34. Kobayashi, Y., Igarashi, T., Takahashi, H. & Higasi, K. Infrared and Raman studies of the dimeric structures of 1,3-dihydroxyacetone, d(+)- and dl-glyceraldehyde. *J. Mol. Struct.* **35**, 85–99 (1976).
35. Jin, T. et al. High-energy aqueous sodium-ion batteries. *Angew. Chem. Int. Ed.* **133**, 12050–12055 (2021).
36. Fong, K. D. et al. The interplay of solvation and polarization effects on ion pairing in nanoconfined electrolytes. *Nano Lett.* **24**, 5024–5030 (2024).
37. Gomes, J. F. et al. Influence of silver on the glycerol electrooxidation over AuAg/C catalysts in alkaline medium: a cyclic voltammetry and in situ FTIR spectroscopy study. *Electrochim. Acta* **144**, 361–368 (2014).
38. Sun, T. et al. A biodegradable polydopamine-derived electrode material for high-capacity and long-life lithium-ion and sodium-ion batteries. *Angew. Chem. Int. Ed.* **55**, 10662–10666 (2016).
39. He, X. et al. A novel highly crystalline $Fe_4(Fe(CN)_6)_3$ concave cube anode material for Li-ion batteries with high capacity and long life. *J. Mater. Chem. A* **7**, 11478–11486 (2019).
40. Yamada, T. et al. In situ seamless magnetic measurements for solid-state electrochemical processes in Prussian blue analogues. *Angew. Chem. Int. Ed.* **52**, 6238–6241 (2013).
41. Xie, B. et al. Achieving long-life Prussian blue analogue cathode for Na-ion batteries via triple-cation lattice substitution and coordinated water capture. *Nano Energy* **61**, 201–210 (2019).
42. Gao, H. & Goodenough, J. B. An aqueous symmetric sodium-ion battery with NASICON-structured $Na_3MnTi(PO_4)_3$. *Angew. Chem. Int. Ed.* **128**, 12960–12964 (2016).
43. Pasta, M. et al. Full open-framework batteries for stationary energy storage. *Nat. Commun.* **5**, 1–9 (2014).
44. Wu, X. et al. Energetic aqueous rechargeable sodium-ion battery based on $Na_2CuFe(CN)_6$-$NaTi_2(PO_4)_3$ intercalation chemistry. *ChemSusChem* **7**, 407–411 (2014).
45. Suo, L. et al. "Water-in-salt" electrolyte makes aqueous sodium-ion battery safe, green, and long-lasting. *Adv. Energy Mater.* **7**, 1701189 (2017).
46. Hou, Z., Li, X., Liang, J., Zhu, Y. & Qian, Y. An aqueous rechargeable sodium ion battery based on a $NaMnO_2$-$NaTi_2(PO_4)_3$ hybrid system for stationary energy storage. *J. Mater. Chem. A* **3**, 1400–1404 (2015).
47. Fernández-Ropero, A. J., Saurel, D., Acebedo, B., Rojo, T. & Casas-Cabanas, M. Electrochemical characterization of $NaFePO_4$ as positive electrode in aqueous sodium-ion batteries. *J. Power Sources* **291**, 40–45 (2015).
48. Wu, X. et al. Vacancy-free Prussian blue nanocrystals with high capacity and superior cyclability for aqueous sodium-ion batteries. *ChemNanoMat* **1**, 188–193 (2015).
49. Chen, J. et al. High-energy-density aqueous sodium-ion batteries enabled by chromium hexacycnochromate anodes. *Chem. Eng. J.* **415**, 129003 (2021).
50. Wan, T. H., Saccoccio, M., Chen, C. & Ciucci, F. Influence of the discretization methods on the distribution of relaxation times deconvolution: implementing radial basis functions with DRTtools. *Electrochim. Acta* **184**, 483–499 (2015).
51. Ravel, B. & Newville, M. ATHENA, ARTEMIS, HEPHAESTUS: data analysis for X-ray absorption spectroscopy using IFEFFIT. *J. Synchrotron Radiat.* **12**, 537–541 (2005).

52. Kresse, G. & Furthmüller, J. Efficiency of ab-initio total energy calculations for metals and semiconductors using a plane-wave basis set. *Comput. Mater. Sci.* **6**, 15–50 (1996).
53. Perdew, J. P., Burke, K. & Ernzerhof, M. Generalized gradient approximation made simple. *Phys. Rev. Lett.* **77**, 3865 (1996).
54. Grimme, S., Antony, J., Ehrlich, S. & Krieg, H. A consistent and accurate ab initio parametrization of density functional dispersion correction (DFT-D) for the 94 elements H-Pu. *J. Chem. Phys.* **132**, 154104 (2010).
55. Grimme, S., Ehrlich, S. & Goerigk, L. Effect of the damping function in dispersion corrected density functional theory. *J. Comput. Chem.* **32**, 1456–1465 (2011).

Acknowledgements

This work was supported by the National Natural Science Foundation (NSFC) of China (52122214, Y.L., 22309083, Q.G., and 52161145503, Q.H.), Jiangsu Province Carbon Peak and Neutrality Innovation Program (Industry tackling on prospect and key technology BE2022002-5, Y.-S.H.), and the Fundamental Research Funds for the Central Universities No. 30923010210 (Q.G.). We thank the 1W1B beamline of Beijing Synchrotron Radiation Facility for support.

Author contributions

Y.-S.H. and Y.L. designed and conceived this project; Q.G. prepared the materials and carried out the electrochemical measurements; R.X. carried out the calculations; Q.G., S.H., J.L., and H.X. performed the EQCM experiments; Q.H. carried out the ex situ XRD and FTIR tests; Y.N. and X. Hou performed the structural refinement; S.H., F.X., and L.Z. carried out the in situ XRD tests; Q.G., X.R., and F.D. carried out the XAS tests and analysis; S.W. and X.W. performed the cryo-STEM tests; Y.Y. performed the XPS tests. Q.G., Y.L., R.X., and Y.-S.H. wrote the manuscript. Y.L., H.L., X. Huang, L.C., and Y.-S.H. reviewed and edited the manuscript. All the authors participated in the analysis and discussions of the experimental results and commented on the manuscript.

Competing interests

The authors declare no competing interests.

Additional information

Supplementary information The online version contains supplementary material available at https://doi.org/10.1038/s41467-025-59980-z.

Correspondence and requests for materials should be addressed to Yaxiang Lu, Ruijuan Xiao or Yong-Sheng Hu.

Peer review information *Nature Communications* thanks Marco Giorgetti, Hyun-Wook Lee, and the other anonymous reviewers for their contribution to the peer review of this work. A peer review file is available.